

Vision Non-Causal Trapezoidal Mamba: Eliminating Directional Scanning in Vision SSMs with Second-Order Dynamics

Anvitha Ramachandran¹ Dhruv Parikh¹

Haoyang Fan¹ Rajgopal Kannan² Viktor Prasanna¹

¹University of Southern California ²DEVCOM Army Research Office

[alramach, dhruvash, prasanna}@usc.edu rajgopal.kannan.civ@army.mil

Abstract

State Space Models (SSMs) have emerged as an alternative to Vision Transformers, yet most vision SSMs inherit directional token scanning from causal sequence modeling. While effective for sequential data, directional scanning introduces spatial bias and orientation-sensitive representations. We present Vision Non-Causal Trapezoidal Mamba (VNCT), a second-order non-causal vision SSM that enables all image tokens to interact in a single pass, eliminating directional scanning and achieving low single-image inference latency. VNCT exhibits more orientation-robust representations, showing reduced performance degradation under image rotations and flips, while improving Boundary IoU by up to 3.7 points, leading to more accurate boundary preservation and object localization. Across ImageNet-1K classification, COCO object detection and instance segmentation, and ADE20K semantic segmentation, VNCT consistently outperforms both directional-scanning vision SSMs and first-order non-causal SSMs. These results show that directional scanning is unnecessary for high-performance vision SSMs and that second-order non-causal state-space modeling offers a simple, efficient, and robust alternative for visual recognition. The code for the model will be made available at <https://github.com/anvitha305/VNCT>.

1. Introduction

State Space Models (SSMs) have emerged as an efficient alternative to Vision Transformers (ViTs) for modeling long-range dependencies with linear-time complexity. Recent advances, including selective state-space models and State Space Duality (SSD), have significantly improved the expressiveness and efficiency of sequence modeling [8, 14]. Building on these developments, vision SSMs such as ViM, VMamba, LocalMamba, and VSSD have demonstrated competitive performance across image classification and dense prediction tasks [23, 31, 43, 65]. These successes have es-

tablished state-space models as a promising family of vision backbones.

Despite their success, most vision SSMs inherit directional token scanning from causal sequence modeling. Because conventional SSMs operate over one-dimensional sequences, image tokens must be serialized through predefined scan paths before state propagation. While effective, directional scanning imposes an artificial traversal order that introduces spatial bias, orientation-sensitive feature interactions, and often requires multiple scan passes to aggregate bidirectional context. These assumptions are fundamentally misaligned with the non-causal nature of visual scenes, where spatial relationships are independent of token ordering. This raises a fundamental question: *is directional scanning necessary for high-performance vision state-space models, or is it simply an artifact of adapting sequence models to images?*

Recent work has begun addressing this limitation through non-causal state-space formulations. In particular, Vision State Space Duality (VSSD) demonstrated that directional scanning can be replaced with global non-causal aggregation while maintaining competitive visual performance [43]. Meanwhile, Mamba-3 introduced second-order exponential-trapezoidal dynamics that substantially improve sequence modeling capability [25]. However, existing non-causal vision SSMs remain limited to first-order dynamics, leaving the potential of second-order non-causal state-space modeling largely unexplored.

We present Vision Non-Causal Trapezoidal (VNCT) Mamba, a hierarchical vision backbone built upon a second-order non-causal state-space formulation. Its core Non-Causal Mamba-3 (NC-M3) layer reformulates the exponential-trapezoidal dynamics of Mamba-3 as a global non-causal aggregation operator, enabling all image tokens to interact in a *single pass* without directional scanning. VNCT further incorporates a low-rank multi-input multi-output (MIMO) parameterization to jointly model spatial and channel-wise interactions. Eliminating directional scanning reduces single-image inference latency while producing

more orientation-robust representations.

We evaluate VNCT on ImageNet-1K classification, COCO object detection and instance segmentation, ADE20K semantic segmentation. VNCT outperforms both directional-scanning vision SSMs and first-order non-causal state-space models. Measured single-image inference latency demonstrates that these gains are achieved without sacrificing deployment efficiency. Furthermore, VNCT exhibits substantially stronger robustness to image rotations and flips and improves Boundary IoU by up to 3.7 points, indicating more accurate boundary preservation and object localization. Together, these results demonstrate that directional scanning is unnecessary for high-performance vision SSMs and that second-order non-causal state-space modeling offers a simple, efficient, robust alternative for visual recognition.

Our contributions are summarized as follows:

- We propose **NC-M3**, a second-order non-causal state-space layer that eliminates directional scanning and enables single-pass interactions among all image tokens.
- We develop **VNCT**, a hierarchical vision backbone that combines second-order non-causal dynamics with a low-rank MIMO parameterization for efficient visual representation learning.
- We demonstrate that eliminating directional scanning improves single-image inference latency, orientation robustness, and boundary preservation while consistently outperforming existing directional-scanning and first-order non-causal vision SSMs across image classification and dense prediction benchmarks.

2. Related Work

2.1. Vision State-Space Backbones and Scanning

State-space models (SSMs) offer a linear-complexity alternative to self-attention, from structured S4 to selective Mamba and Mamba-2/SSD [8, 14, 15], and their vision extensions rival CNNs and Vision Transformers on classification and dense prediction [23, 31, 40, 44, 55, 65]. All inherit the causal one-dimensional recurrence of sequence models, flattening images along horizontal, vertical, local, or multi-directional scan paths that impose a spatial order not intrinsic to visual data. Follow-up work—DAMamba, DefMamba, QuadMamba, GroupMamba, SF-Mamba—improves these scans through adaptive, deformable, quadtree, grouped, or token-swapped routing rather than removing them [26, 30, 42, 54, 58], confirming that scan order is a central bottleneck yet still treating vision as ordered traversal. VNCT instead eliminates the traversal: its NC-M3 operator aggregates over all image tokens through a scan-order-independent, non-causal computation.

2.2. Scan-Free and Non-Causal Vision SSMs

The closest prior work removes the causal mask altogether. VSSD introduced a non-causal form of State Space Duality for vision, replacing per-token causal hidden states with a shared global state [43]; while a relevant work, it is built on first-order Mamba-2/SSD dynamics with a SISO-style parameterization, whereas VNCT lifts Mamba-3’s second-order exponential-trapezoidal dynamics into the non-causal setting and additionally introduces low-rank MIMO state mixing. Other scan-reducing designs—Spatial-Mamba’s dilated local state fusion, Mamba2D’s causal wavefront recurrence, and PRISMamba’s concentric-ring averaging, alongside non-SSM mixers such as SEMA and HAMSA—either retain a residual scan or abandon the state-space view [2, 21, 39, 50, 52]. VNCT alone preserves a structured SSM interpretation, parameterizing global aggregation by second-order SSM coefficients rather than convolutional fusion, unweighted averaging, or spectral multiplication.

2.3. Operator Expressivity and Global Mixing

VNCT builds on Mamba-3’s enrichment of State Space Duality with exponential-trapezoidal discretization, complex-valued updates, and a MIMO formulation [8, 25], whose second-order left/right-endpoint update generalizes the exponential-Euler step of Mamba-1/2 and aligns with evidence that richer transitions improve SSM expressivity [13, 37]. Computing global source statistics followed by per-token readout makes the operator algebraically linear-attention-like [17, 24], but its kernel is fixed by data-dependent SSM coefficients (α, β, γ) rather than free query-key projections; where RALA treats low rank as the bottleneck of linear attention [11], VNCT resolves it through MIMO cross-channel coupling from within the SSM. Against hybrids that interleave SSM and attention modules [12, 19, 35] and MambaOut’s claim that Mamba is unnecessary for visual recognition [59], VNCT contends that the limitation is the causal directional scan, not state-space modeling itself—so it retains the SSM, strengthens it with second-order non-causal dynamics, and confines self-attention to the final low-resolution stage.

3. Methodology

3.1. Overview

Existing vision SSMs process images through directional token scanning, introducing an artificial traversal order that biases spatial interactions and often requires multiple scan passes [31, 43, 65]. We propose VNCT (Vision Non-Causal Trapezoidal Mamba), a hierarchical vision backbone built on a non-causal reformulation of the second-order exponential-trapezoidal dynamics of Mamba-3 [25]. The core *non-causal lift* transforms the causal Mamba-3 recurrence into a globally factorized, permutation-invariant aggregation operator,

enabling all image tokens to interact in a single pass without directional scanning. The resulting **NC-M3** layer incorporates input-dependent state parameterization, 2D rotary positional encoding, and an optional low-rank MIMO state-mixing mechanism, and is stacked into a four-stage hierarchical backbone for classification, detection, instance segmentation, and semantic segmentation.

3.2. Preliminaries

3.2.1. Linear State-Space Models

Let $\mathbf{X} = [\mathbf{x}_1, \dots, \mathbf{x}_L]^\top \in \mathbb{R}^{L \times C}$ denote L image tokens with channel dimension C , and let $\mathbf{H} \in \mathbb{R}^{L \times C}$ be the output sequence. A continuous-time linear SSM evolves a latent state $\mathbf{h}(t)$ as

$$\dot{\mathbf{h}}(t) = \mathbf{A}\mathbf{h}(t) + \mathbf{b}x(t), \quad y(t) = \mathbf{E}\mathbf{h}(t) + D x(t). \quad (1)$$

Zero-order-hold (ZOH) discretization with step Δ yields

$$\mathbf{h}_t = \underbrace{\exp(\Delta\mathbf{A})}_{\boldsymbol{\alpha}_t} \mathbf{h}_{t-1} + \underbrace{(\Delta\mathbf{A})^{-1}(\exp(\Delta\mathbf{A}) - \mathbf{I})\Delta\mathbf{b}}_{\boldsymbol{\beta}_t} x_t. \quad (2)$$

Efficient architectures such as S4 [15], Mamba [14], and Mamba-2 [8] restrict \mathbf{A} to diagonal form. The sequential structure of Eq. (2) encodes only the prefix $\{x_1, \dots, x_t\}$ at each position, introducing scan anisotropy when applied to 2D visual inputs.

3.2.2. Mamba-3 and Second-Order State Dynamics

Mamba-3 [25] replaces ZOH with trapezoidal quadrature, averaging over both integration endpoints:

$$\mathbf{h}_t = \boldsymbol{\alpha}_t \mathbf{h}_{t-1} + \boldsymbol{\beta}_t x_{t-1} + \boldsymbol{\gamma}_t x_t, \quad (3)$$

where $\boldsymbol{\beta}_t$ and $\boldsymbol{\gamma}_t$ weight the left- and right-endpoint observations respectively. This second-order correction induces a richer implicit convolutional kernel and improves sequence modeling quality [25], but the recurrence remains causal, enforcing a scan trajectory on visual inputs. VNCT derives an equivalent order-independent formulation of Eq. (3)'s information-mixing behavior, described next.

3.3. Non-Causal Lift of Trapezoidal State Dynamics

The goal is to construct a permutation-invariant operator

$$\mathbf{H} = \mathcal{F}_{\text{NC}}(\mathbf{X}), \quad \mathbf{H} \in \mathbb{R}^{L \times C}, \quad (4)$$

that captures the information-mixing behavior of Eq. (3) while permitting fully parallel, order-independent evaluation. The *non-causal lift* preserves the roles of $\boldsymbol{\alpha}$, $\boldsymbol{\beta}$, $\boldsymbol{\gamma}$ as interaction coefficients while discarding sequential state dependence and scan ordering.

3.3.1. Kernel Formulation of the Non-Causal Interaction

We replace the lower-triangular causal transition matrix with a fully dense, normalized interaction kernel. For output location i , source location j , and channel c :

$$\mathcal{W}_{ij,c} = \frac{\phi(\boldsymbol{\alpha}_{i,c})^\top \psi(\boldsymbol{\beta}_{j,c} + \boldsymbol{\gamma}_{j,c})}{\sum_{k=1}^L \phi(\boldsymbol{\alpha}_{i,c})^\top \psi(\boldsymbol{\beta}_{k,c} + \boldsymbol{\gamma}_{k,c})}, \quad (5)$$

where $\phi, \psi : \mathbb{R}^D \rightarrow \mathbb{R}_{\geq 0}^D$ are positive-valued feature maps projecting SSM parameters into a D -dimensional interaction space. Here $\phi(\boldsymbol{\alpha}_{i,c})$ acts as a query controlling context aggregation range — large $\boldsymbol{\alpha}$ (slow decay) produces large-norm queries while small $\boldsymbol{\alpha}$ (rapid decay) yields near-local outputs — preserving the semantic role of $\boldsymbol{\alpha}$ as a memory-length controller. The source term $\boldsymbol{\beta}_{j,c} + \boldsymbol{\gamma}_{j,c}$ combines both trapezoidal endpoints and depends only on index j , enabling precomputation independently of i for the linear-time factorization below. The denominator ensures $\sum_j \mathcal{W}_{ij,c} = 1$.

Factoring $\phi(\boldsymbol{\alpha}_{i,c})$ out of the source sums gives the aggregation rule

$$\begin{aligned} h_{i,c} &= \sum_{j=1}^L \mathcal{W}_{ij,c} \tilde{x}_{j,c} \\ &= \frac{\phi(\boldsymbol{\alpha}_{i,c})^\top \sum_{j=1}^L \psi(\boldsymbol{\beta}_{j,c} + \boldsymbol{\gamma}_{j,c}) \tilde{x}_{j,c}}{\phi(\boldsymbol{\alpha}_{i,c})^\top \sum_{k=1}^L \psi(\boldsymbol{\beta}_{k,c} + \boldsymbol{\gamma}_{k,c})}, \end{aligned} \quad (6)$$

where $\tilde{x}_{j,c} = b_{j,c} x_{j,c}$. Although algebraically similar to linear attention [5, 24], ϕ and ψ here operate on SSM discretization parameters rather than arbitrary input features, inheriting the inductive biases of the Mamba-3 parameterization.

3.3.2. Factorized Global Aggregation

The inner sums in Eq. (6) are independent of i , enabling linear-time computation via global sufficient statistics

$$\mathbf{S}_c = \sum_{j=1}^L \psi(\boldsymbol{\beta}_{j,c} + \boldsymbol{\gamma}_{j,c}) \tilde{x}_{j,c}, \quad (7)$$

$$\mathbf{Z}_c = \sum_{j=1}^L \psi(\boldsymbol{\beta}_{j,c} + \boldsymbol{\gamma}_{j,c}), \quad (8)$$

with $\mathbf{S}_c, \mathbf{Z}_c \in \mathbb{R}^D$ summarizing the entire token set independently of any output index. The aggregation reduces to

$$h_{i,c} = \frac{\phi(\boldsymbol{\alpha}_{i,c})^\top \mathbf{S}_c}{\phi(\boldsymbol{\alpha}_{i,c})^\top \mathbf{Z}_c}. \quad (9)$$

Computation decomposes into two $\mathcal{O}(LD)$ passes: a source-side pass accumulating $(\mathbf{S}_c, \mathbf{Z}_c)$ and a target-side pass evaluating $h_{i,c}$ for all i simultaneously, without ever constructing the $L \times L$ interaction matrix.

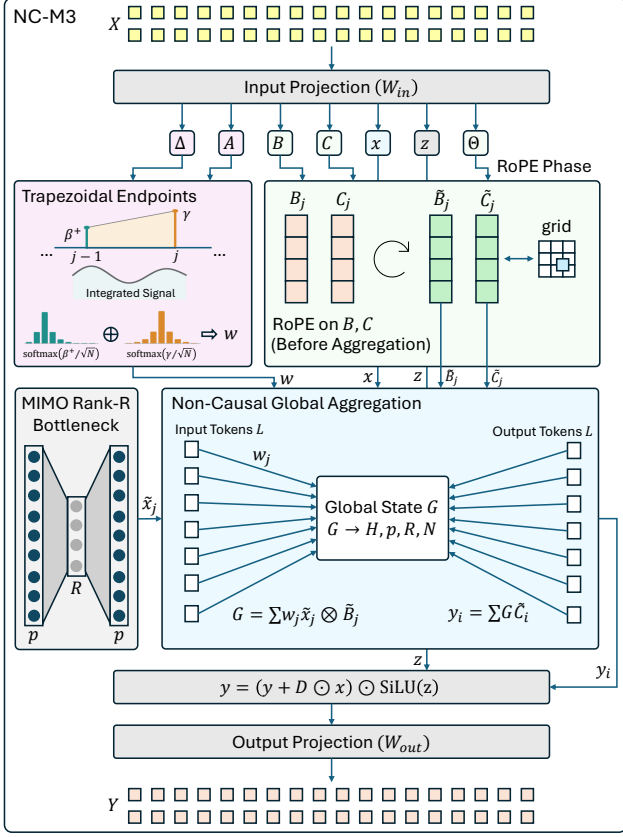


Figure 1. **The NC-M3 block.** Input tokens are projected into value, key/query, gating, and second-order state-parameter streams. Trapezoidal endpoints form the fused source weight w and 2D RoPE injects geometry into \mathbf{B} , \mathbf{C} ; all tokens then aggregate into a single global state \mathbf{G} that every output token reads back, yielding scan-free, linear-time global mixing.

3.4. NC-M3: Non-Causal Mamba-3 Block

The NC-M3 block (Fig. 1) instantiates Eqs. (7)–(9) within a full feature transformation pipeline. Given input tokens $\mathbf{X} \in \mathbb{R}^{L \times C}$, NC-M3 produces output tokens $\mathbf{Y} \in \mathbb{R}^{L \times C}$, following the structural conventions of Mamba and Mamba-2 [8, 14]: expanded inner dimension, parallel gating and value streams, input-dependent state parameters, and skip-connection output.

3.4.1. Input Projection and State Parameter Generation

A single linear projection expands the C -dimensional input into all required streams:

$$[\mathbf{z}, \mathbf{x}, \mathbf{B}, \mathbf{C}, \Delta, \Lambda, \Theta] = \mathbf{X}\mathbf{W}_{in}^T + \mathbf{b}_{in}, \quad (10)$$

with total projected dimension $d_{in} = 2d_{inner} + 2NR + 3H + S$, where $d_{inner} = 2C$, N is the SSM state dimension, H the number of SSM heads, R the MIMO rank, and S the number of RoPE angle dimensions. Here \mathbf{z} is the gate stream, \mathbf{x}

the value stream, \mathbf{B} the source projection (ψ in Eq. (5)), \mathbf{C} the query projection (ϕ in Eq. (5)), Δ the data-dependent step-size logit, Λ the trapezoidal interpolation logit, and Θ the RoPE angle stream.

From the projected streams, the three SSM parameters of Eq. (3) are computed as data-dependent, per-head quantities:

$$DT_{i,h} = \text{softplus}(\Delta_{i,h} + b_{\Delta,h}), \quad DT \in \mathbb{R}^{L \times H}, \quad (11)$$

with $A_h = -\text{softplus}(a_h)$ constraining the learned head-wise decay negative. The three SSM parameters are then

$$\alpha_{i,h} = \exp(A_h \cdot DT_{i,h}), \quad (12)$$

$$\gamma_{i,h} = \sigma(\Lambda_{i,h}) \cdot DT_{i,h}, \quad (13)$$

$$\beta_{i,h} = (1 - \sigma(\Lambda_{i,h})) \cdot DT_{i,h} \cdot \alpha_{i,h}, \quad (14)$$

where $\sigma(\cdot)$ is the sigmoid. Since $A_h < 0$ and $DT_{i,h} > 0$, $\alpha_{i,h} \in (0, 1)$. The sigmoid-gated logit partitions $DT_{i,h}$ into complementary right-endpoint weight γ (fraction $\sigma(\Lambda)$) and left-endpoint weight β (fraction $1 - \sigma(\Lambda)$, scaled by α), recovering the Mamba-3 trapezoidal discretization.

3.4.2. Direction-Agnostic Global Aggregation

Since Eq. (9) is permutation invariant, spatial information is injected via 2D rotary positional encoding (RoPE) [45] applied to the source and query projections \mathbf{B} and \mathbf{C} , encoding relative spatial displacement while preserving the linear-time factorization (see Supplement A.4). The fused source weight realizing $\psi(\beta_{j,c} + \gamma_{j,c})$ is

$$w_{j,h} = \text{softmax}_L(\gamma_{j,h}/\sqrt{N}) + \text{softmax}_L(\beta_{j,h}^+/\sqrt{N}), \quad (15)$$

where $\beta_{j,h}^+ = \beta_{j+1,h}$ is the one-step-ahead roll of β . The two softmax terms correspond to the trapezoidal integration endpoints, yielding a constant normalization term in Eq. (9).

NC-M3 optionally employs a low-rank MIMO formulation for cross-head interaction at $\mathcal{O}(CR)$ cost. The value stream is expanded as

$$\tilde{x}_{i,h,p,r} = \sum_{p'} x_{i,h,p'} U_{h,r,p'}, \quad (16)$$

followed by global accumulation and readout:

$$\mathbf{G}_{h,p,r,n} = \sum_{j=1}^L w_{j,h} \tilde{x}_{j,h,p,r} \tilde{B}_{j,r,n}, \quad (17)$$

$$y_{i,h,p} = \sum_{r,n} \mathbf{G}_{h,p,r,n} \tilde{C}_{i,r,n}. \quad (18)$$

The global state tensor \mathbf{G} is computed once and reused for all tokens, preserving $\mathcal{O}(LCR)$ overall complexity. MIMO is evaluated in the ablation studies (Section 4).

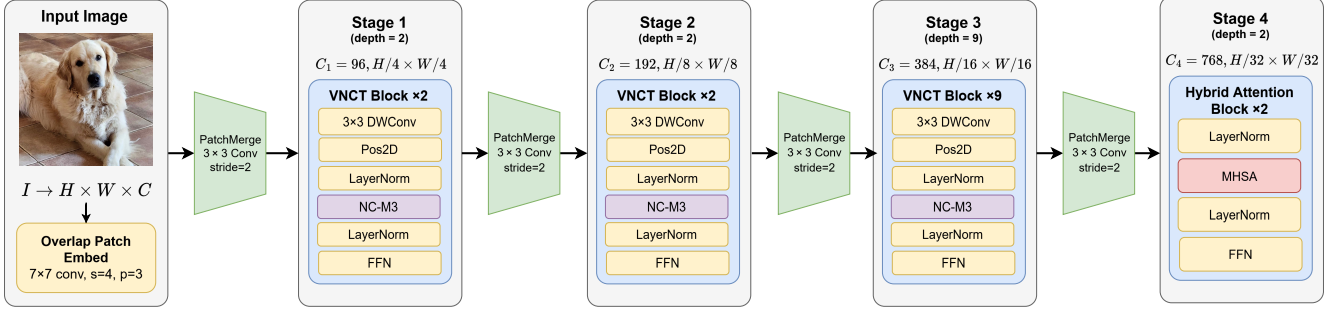


Figure 2. **Overview of the VNCT backbone.** The input image is processed through a four-stage hierarchical architecture with progressive spatial downsampling and increasing channel dimensions. Stages 1–3 employ VNCT blocks based on the proposed NC-M3 layer, while Stage 4 uses Hybrid-Attention. Multi-scale features are produced for downstream dense prediction tasks, and the final stage is globally pooled for image classification.

3.4.3. Output Projection and Residual Update

Following the readout of Eq. (18), a per-head skip connection and gated non-linearity are applied:

$$\mathbf{y} = (\mathbf{h} + \mathbf{D} \odot \mathbf{x}) \odot \text{SiLU}(\mathbf{z}), \quad (19)$$

where \mathbf{h} is the readout, $\mathbf{D} \in \mathbb{R}^H$ is a per-head learnable skip coefficient, \mathbf{x} the value stream, and \mathbf{z} the gate stream. After gating, \mathbf{y} is reshaped and projected back to the input dimension:

$$\mathbf{Y} = \mathbf{y} \mathbf{W}_{\text{out}}^T, \quad \mathbf{W}_{\text{out}} \in \mathbb{R}^{C \times d_{\text{inner}}}, \quad (20)$$

with $\mathbf{Y} \in \mathbb{R}^{L \times C}$ returned as the SSM branch contribution in Eq. (24).

3.5. VNCT Backbone Architecture

3.5.1. Hierarchical Architecture

VNCT adopts a four-stage hierarchical architecture (Fig. 2) with progressively decreasing spatial resolution and increasing channel width. An overlapping patch embedding (7×7 conv, stride 4, padding 3, LayerNorm) yields

$$\mathbf{X}_1 \in \mathbb{R}^{\frac{H_{\text{in}}}{4} \times \frac{W_{\text{in}}}{4} \times C_1}, \quad (21)$$

and each subsequent stage applies a 3×3 strided convolution to halve spatial resolution and double the channel dimension. Detailed configurations for all VNCT variants are provided in the supplementary material.

3.5.2. VNCT Block

Each VNCT block (Stages 1–3) applies four components in sequence. First, a Local Perception Unit (LPU) injects local spatial inductive bias:

$$\mathbf{x}' = \mathbf{x} + \text{LN}(\text{DWConv}_{3 \times 3}(\mathbf{x})). \quad (22)$$

2D sinusoidal positional encoding is then added:

$$\mathbf{x}'' = \mathbf{x}' + \text{Pos2D}(\mathbf{x}', H, W). \quad (23)$$

Global interaction is performed by NC-M3 with a layer-scaled residual:

$$\mathbf{x}''' = \mathbf{x}'' + \lambda_1 \odot \text{NC-M3}(\text{LN}(\mathbf{x}''), H, W), \quad (24)$$

where λ_1 is initialized to 10^{-5} [49]. A two-layer FFN with layer-scaled residual and stochastic depth [22] completes the block:

$$\mathbf{x}_{\text{out}} = \mathbf{x}''' + \lambda_2 \odot \text{FFN}(\text{LN}(\mathbf{x}''')). \quad (25)$$

3.5.3. Multi-Scale Representation

Stage 4 replaces NC-M3 with multi-head self-attention (MHSA), restricting quadratic attention to the lowest-resolution feature map where its cost is negligible. The four stages yield a feature pyramid at strides $\{4, 8, 16, 32\}$, making VNCT directly compatible with UPerNet [53], FPN [28], Mask R-CNN [20], and standard classification heads.

4. Experiments

4.1. Implementation Details

Unless otherwise specified, all experiments are implemented in PyTorch and trained on 8 NVIDIA RTX 6000 Ada GPUs using Distributed Data Parallel with automatic mixed precision. ImageNet-1K models are trained using a standard AdamW-based recipe with common data augmentation strategies [7, 33, 34, 46, 48, 60–62]. For downstream detection, instance segmentation, and semantic segmentation, we follow the official VSSD training protocols [43] using Mask R-CNN [20] in MMDetection and UPerNet [53] in MMsegmentation, initializing all backbones from ImageNet-1K pretrained checkpoints. Complete hyperparameters are provided in the supplementary material.

4.2. Image Classification on ImageNet-1K

Experimental Setup. We evaluate VNCT on ImageNet-1K [9] using standard Top-1 accuracy across micro, tiny,

Table 1. **ImageNet-1K classification (Micro and Tiny models)**. Top-1 accuracy (%) on the ImageNet-1K validation set. Method types: Conv (convolutional), Attn (attention-based), SSM (scan-based state-space), SSD (first-order non-causal state-space), NCT (second-order non-causal, ours). Parameter counts and FLOPs are for the classification backbone only. VNCT achieves the best Top-1 accuracy at both scales.

Method	Type	#Param.	FLOPs	Top-1
Micro Models				
RegNetY-1.6G [41]	Conv	11M	1.6G	78.0
EffNet-B3 [47]	Conv	12M	1.8G	81.6
PVTv2-b1 [51]	Attn	13M	2.1G	78.7
BiFormer [64]	Attn	13M	2.2G	81.4
NAT-M [18]	Attn	20M	2.7G	81.8
SMT-T [29]	Attn	12M	2.4G	82.2
Vim-T [65]	SSM	7M	1.5G	76.1
LVim-T [23]	SSM	8M	1.5G	76.2
VSSD-M [43]	SSD	14M	2.3G	82.5
VNCT-Micro	NCT	15M	2.5G	83.3
Tiny Models				
ConvNeXt-T [33]	Conv	29M	4.5G	82.1
MambaOut-T [59]	Conv	27M	4.5G	82.7
EffNet-B4 [47]	Conv	19M	4.2G	82.9
Swin-T [32]	Attn	29M	4.5G	81.3
PVTv2-B2 [51]	Attn	25M	4.0G	82.0
NAT-T [18]	Attn	28M	4.3G	83.2
VMambaV9-T [31]	SSM	31M	4.9G	82.5
MSVMamba-T [44]	SSM	33M	4.6G	82.8
VSSD-T [43]	SSD	24M	4.5G	83.7
VNCT-Tiny	NCT	28M	5.0G	84.2

small, and base model scales, comparing against representative CNNs, Vision Transformers, directional-scanning SSMs, and recent non-causal state-space models. We additionally report single-image FP16 inference latency on the same hardware to assess practical deployment efficiency (Table 3).

Results and Discussion. VNCT consistently achieves the strongest classification performance at all evaluated scales (Tables 1, 2), improving upon both scan-based baselines (VMamba, LocalVMamba) and the first-order non-causal baseline (VSSD). These results demonstrate that directional sequential scanning is unnecessary for competitive visual representations, and that the proposed second-order dynamics provide additional representational capacity over first-order formulations. Accuracy gains are achieved without sacrificing efficiency: VNCT attains lower latency than VSSD at the Micro, Tiny, and Small scales and remains competitive at Base scale (Table 3).

4.3. Object Detection and Instance Segmentation on COCO

Experimental Setup. We evaluate on MS COCO [27] using Mask R-CNN [20] in MMDetection [3], following the protocol of prior work [31, 32].

Results and Discussion. VNCT consistently improves both box and mask AP over all Vision Mamba architectures (Table 4). The largest gains appear at AP₇₅, indicating improved localization precision. Improvements across both detection

Table 2. **ImageNet-1K classification (Small and Base models)**. Top-1 accuracy (%) at larger model scales. VNCT-Small achieves state-of-the-art accuracy with fewer FLOPs than VMamba-S; VNCT-Base surpasses VSSD-B while using fewer parameters and FLOPs. See Table 1 for type abbreviations.

Method	Type	#Param.	FLOPs	Top-1
Small Models				
ConvNeXt-S [33]	Conv	50M	8.7G	83.1
MambaOut-S [59]	Conv	48M	9.0G	84.1
Swin-S [32]	Attn	50M	8.7G	83.0
VMamba-S [31]	SSM	44M	11.2G	83.5
VSSD-S [43]	SSD	40M	7.4G	84.5
VNCT-Small	NCT	44M	8.0G	84.7
Base Models				
ConvNeXt-B [33]	Conv	89M	15.4G	83.8
MambaOut-B [59]	Conv	85M	15.8G	84.2
Swin-B [32]	Attn	88M	15.4G	83.5
VMambaV9-B [31]	SSM	89M	15.4G	83.9
VSSD-B [43]	SSD	89M	16.1G	85.4
VNCT-Base	NCT	86M	15.5G	85.6

Table 3. **Single-image FP16 inference latency (ms/image)**. Measured on a single NVIDIA RTX 6000 Ada GPU at batch size 1 with 224×224 inputs. FLOPs measure theoretical complexity but do not reflect wall-clock speed; latency directly captures deployment efficiency under a standardized setting. VNCT achieves lower latency than VSSD at Micro, Tiny, and Small scales by replacing directional scan passes with shared global sufficient statistics, and remains competitive at Base scale.

Micro		Tiny	
Method	ms/img	Method	ms/img
EffNet-B3	4.40	ConvNeXt-T	7.27
VSSD-M	5.80	Swin-T	8.43
VNCT-Micro	5.25	VMamba-T	10.09
		VSSD-T	8.01
		VNCT-Tiny	7.31
Small		Base	
Method	ms/img	Method	ms/img
ConvNeXt-S	13.03	ConvNeXt-B	21.25
VMamba-S	18.31	VMamba-B	27.33
VSSD-S	13.24	VSSD-B	23.19
VNCT-Small	12.35	VNCT-Base	22.10

and segmentation suggest that global non-causal aggregation and second-order state dynamics yield stronger spatial representations for dense prediction.

4.4. Semantic Segmentation on ADE20K

Experimental Setup. We evaluate semantic segmentation on ADE20K [63] with the UPerNet decoder [53] in MMsegmentation [6], reporting mIoU under single-scale (SS) and multi-scale (MS) evaluation.

Results and Discussion. VNCT achieves the strongest segmentation performance among comparable state-space backbones at all model scales (Table 5). Consistent improvements over other SSM-based architectures indicate that the gains are not solely attributable to removing directional scan-

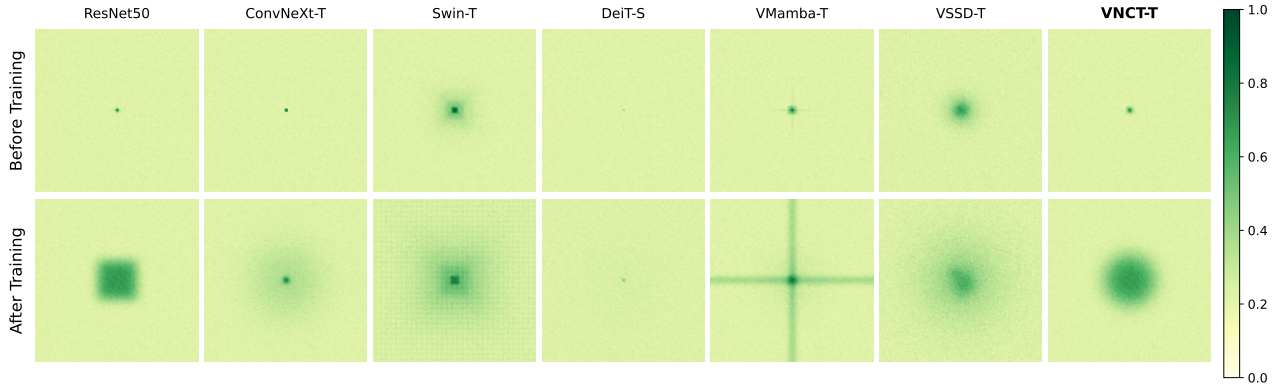


Figure 3. **Effective Receptive Field (ERF) maps before and after training.** Spatial gradient energy of the central pixel with respect to the input image, averaged over the ImageNet-1K validation set using the gradient-based method of [36]; values normalized to $[0, 1]$. Seven representative backbones are compared: CNN-based (ResNet-50, ConvNeXt-T), attention-based (Swin-T, DeiT-S), and SSM-based (VMamba-T, VSSD-T, VNCT-T). CNNs produce localized receptive fields due to finite convolutional kernels; DeiT-S shows a centralized high-response region with weak global activation; VMamba-T exhibits prominent horizontal/vertical artifacts from directional scan-based state propagation; VSSD-T substantially enlarges coverage but remains irregular and asymmetric. VNCT-T uniquely achieves a smooth, symmetric, and uniformly distributed receptive field spanning the entire image, reflecting isotropic long-range propagation without directional scanning or attention.

Table 4. **Object detection and instance segmentation with Mask R-CNN on MS COCO [27].** Box AP (AP^b) and mask AP (AP^m) under $1\times$ and $3\times$ +MS (multi-scale) training schedules; subscripts 50 and 75 denote IoU thresholds. Protocol: shorter side 800 px, longer side ≤ 1333 px, AdamW with $lr 1 \times 10^{-4}$, batch size 16. VNCT-T surpasses all baselines on every metric at both schedules, with the largest gains at AP_{75}^m .

Method	$1\times$						$3\times + MS$					
	AP^b	AP_{50}^b	AP_{75}^b	AP^m	AP_{50}^m	AP_{75}^m	AP^b	AP_{50}^b	AP_{75}^b	AP^m	AP_{50}^m	AP_{75}^m
Swin-T [32]	42.7	65.2	46.8	39.3	62.2	42.2	46.0	68.1	50.3	41.6	65.1	44.9
ConvNeXt-T [33]	44.2	66.6	48.3	40.1	63.3	42.8	46.2	67.9	50.8	41.7	65.0	44.9
VMamba-T [31]	46.5	68.5	50.7	42.1	65.5	45.3	48.5	69.9	52.9	43.2	66.8	46.3
LocalVMamba-T [23]	46.7	68.7	50.8	42.2	65.7	45.5	48.7	70.1	53.0	43.4	67.0	46.4
VSSD-T [43]	46.9	69.4	51.4	42.6	66.4	45.9	48.8	70.4	53.4	43.6	67.6	46.9
VNCT-T	47.8	70.3	52.6	43.5	67.3	46.8	49.7	71.3	54.6	44.5	68.6	47.9

ning; the results further suggest that second-order non-causal dynamics are particularly beneficial for dense scene understanding and fine-grained spatial modeling.

4.5. Effective Receptive Field Visualization

Experimental Setup. We visualize the Effective Receptive Field (ERF) following [36], computing the gradient magnitude of the central pixel with respect to the input across the ImageNet-1K validation set, both before and after training.

Results and Discussion. The ERF maps in Fig. 3 reveal the distinct spatial inductive biases of each architecture. VNCT-T is the only model to produce a smooth, symmetric, and globally uniform receptive field, indicating that the proposed second-order exponential-trapezoidal dynamics promote balanced long-range information propagation without directional scans or global attention.

Table 5. **Semantic segmentation on ADE20K [63] with UPerNet [53].** Mean Intersection-over-Union (mIoU, %) under single-scale (SS) and multi-scale (MS) evaluation. All backbones initialized from ImageNet-1K pretrained checkpoints and trained for 160K iterations under identical optimization settings in MMsegmentation [6]. Parameter and FLOPs counts include the UPerNet decoder. VNCT achieves the highest mIoU at all three model scales (Micro, Tiny, Small), consistently outperforming both scan-based and first-order non-causal SSM backbones.

Method	mIoU (SS)	mIoU (MS)	#Param.	FLOPs
EffVMamba-S [40]	41.5	42.1	29M	505G
MSVMamba-M [44]	45.1	45.4	42M	875G
VSSD-M [43]	45.6	46.0	42M	893G
VNCT-M	46.5	47.0	43M	900G
Swin-T [32]	44.4	45.8	60M	945G
ConvNeXt-T [33]	46.0	46.7	60M	939G
VMamba-T [31]	47.3	48.3	55M	964G
LocalVMamba-T [23]	47.9	49.1	57M	970G
EffVMamba-B [40]	46.5	47.3	65M	930G
MSVMamba-T [44]	47.6	48.5	65M	942G
VSSD-T [43]	47.9	48.7	53M	941G
VNCT-T	48.8	49.7	54M	950G
Swin-S [32]	47.6	49.5	81M	1038G
VMamba-S [31]	49.5	50.5	76M	1081G
VSSD-S [43]	49.2	50.1	69M	1002G
VNCT-S	50.1	51.2	44M	1015G

4.6. Orientation Robustness on ImageNet-1K

Experimental Setup. We assess model robustness under common geometric transformations of the ImageNet-1K validation set without additional training or test-time adaptation.

Results and Discussion. VNCT exhibits the strongest robustness across all transformations and the smallest average accuracy drop (Table 6). The reduced degradation under flips

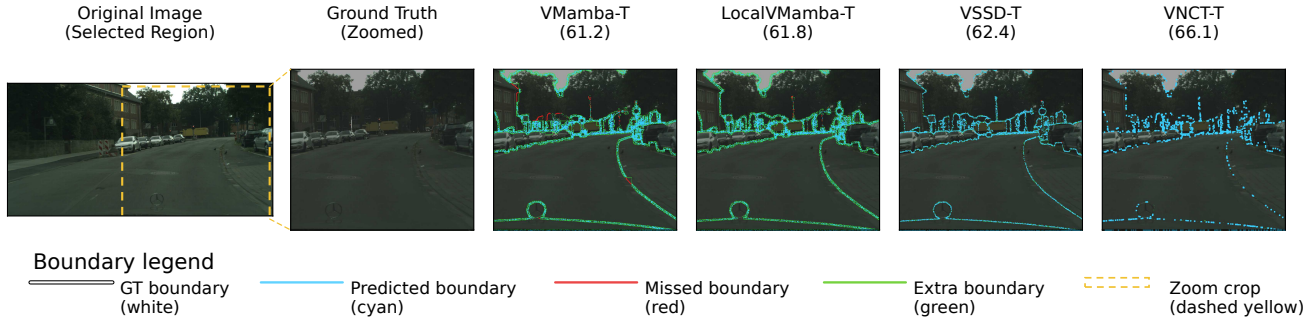


Figure 4. **Qualitative boundary predictions on Cityscapes.** A road-scene crop comparing boundary outputs for VMamba-T, LocalVMamba-T, VSSD-T, and VNCT-T against the ground-truth contour. Color code: cyan = correctly predicted boundaries; red = missed boundaries; green = spurious boundaries. Yellow dashed box indicates the zoomed region. VNCT-T produces the most complete and geometrically accurate contour alignment, consistent with its superior BIoU scores in Table 7.

Table 6. **Orientation robustness on the ImageNet-1K validation set.** Top-1 accuracy (%) evaluated without retraining or test-time adaptation under four geometric transformations: Horizontal Flip (HF), Vertical Flip (VF), 90° Rotation (R90), and 180° Rotation (R180). Avg. Drop: mean accuracy decrease across all four variants relative to the original images; lower is better and indicates reduced orientation sensitivity. VNCT-T achieves the highest accuracy on every variant and the smallest average drop (0.3%), compared to VSSD-T (0.9%) and VMamba-T (1.6%), demonstrating more isotropic spatial representations attributable to both the removal of directional scanning and the second-order non-causal dynamics.

Method	Orig.	HF	VF	R90	R180	Avg. Drop
VMamba-T [31]	82.5	82.1	80.8	79.6	81.0	1.6
VSSD-T [43]	83.7	83.4	82.7	81.9	82.8	0.9
VNCT-T	84.2	84.1	83.9	83.5	83.9	0.3

and rotations confirms that learned representations are less orientation-sensitive; comparison with VSSD further indicates that improved robustness stems not only from removing directional scans but also from the proposed second-order non-causal dynamics.

4.7. Boundary-Sensitivity Evaluation

Experimental Setup. Region-based metrics (AP, mIoU) primarily measure area overlap and may not fully capture contour quality. Following Cheng *et al.* [4], we additionally report Boundary IoU (BIOU) on ADE20K and Cityscapes to evaluate prediction quality near object contours.

Results and Discussion. VNCT-T achieves highest BIOU on both benchmarks (Table 7), with gains of +2.3 and +3.7 BIOU over VSSD-T on ADE20K and Cityscapes, respectively. These gains complement the mIoU improvements and confirm that second-order non-causal dynamics enhance fine-grained contour localization alongside semantic region prediction. Qualitative results in Fig. 4 illustrate the sharper and more complete boundary alignment achieved by VNCT.

Table 7. **Boundary IoU (BIOU) on ADE20K and Cityscapes.** BIOU [4] evaluates segmentation quality near object contours, complementing region-based metrics (mIoU, AP) that primarily measure area overlap. Higher is better. VNCT-T outperforms all Mamba-based baselines on both datasets, with gains of +2.3 and +3.7 BIOU over VSSD-T on ADE20K and Cityscapes, respectively.

Method	ADE20K	Cityscapes
VMamba-T [31]	48.3	61.2
LocalVMamba-T [23]	48.7	61.8
VSSD-T [43]	49.1	62.4
VNCT-T	51.4	66.1

Table 8. **Principal ablations on VNCT-T.** *Left:* core components, evaluated across all tasks—Top-1 (%), ImageNet-1K), box AP (COCO 1×), and mIoU/BIOU (%), ADE20K). *Right:* positional encoding and state dynamics, evaluated on Top-1 and mIoU. Best per group in **bold**.

<i>Core Components</i>					<i>Positional Encoding</i>		
Variant	Top-1	AP	mIoU	BIOU	Variant	Top-1	mIoU
Scan	83.5	46.4	47.6	48.9	None	82.9	46.8
SISO	83.8	47.0	48.0	49.5	2D Sin.	83.7	48.0
VNCT	84.2	47.8	48.8	50.8	RoPE	83.8	48.1
					2D Sin.+RoPE	84.2	48.8
<i>State Dynamics</i>							
					VSSD-T (1st)	83.7	47.9
					VNCT-T (2nd)	84.2	48.8

4.8. Ablation Studies

Unless otherwise specified, all ablations use the VNCT-T backbone. Table 8 summarizes the principal design ablations. Each proposed component contributes to the final performance, with the largest gains arising from non-causal aggregation and the proposed second-order state dynamics. Additional ablations and details are in Supplement A.11.

5. Conclusion

We revisit assumption that vision state-space models require the directional scanning inherited from sequence modeling, and show they do not: pairing scan-free global aggregation with second-order trapezoidal dynamics, VNCT improves recognition, dense prediction, boundary quality at efficient inference. This motivates non-causal, higher-order state-space operators as promising direction for vision backbones.

References

- [1] Tushar Anand, Advik Sinha, and Abhijit Das. Denseperceptncssd: Vision mamba towards real-time dense visual perception with non-causal state space duality. *arXiv.org*, 2025. 12
- [2] Enis Baty, A. Hernández-Díaz, C. Bridges, Rebecca Davidson, Steve Eckersley, and Simon Hadfield. Mamba2d: a natively multi-dimensional state-space model for vision tasks. *arXiv.org*, 2024. 2, 12
- [3] Kai Chen, Jiaqi Wang, Jiangmiao Pang, Yuhang Cao, Yu Xiong, Xiaoxiao Li, Shuyang Sun, Wansen Feng, Ziwei Liu, Jiarui Xu, et al. Mmdetection: Open mmlab detection toolbox and benchmark. *arXiv.org*, 2019. 6
- [4] Bowen Cheng, Ross B. Girshick, Piotr Dollár, A. Berg, and A. Kirillov. Boundary iou: Improving object-centric image segmentation evaluation. In *Computer Vision and Pattern Recognition*, pages 15329–15337. IEEE, 2021. 8
- [5] K. Choromanski, Valerii Likhoshesterov, David Dohan, Xingyou Song, Andreea Gane, Tamás Szepesvári, Peter G. Hawkins, Jared Davis, Afroz Mohiuddin, Lukasz Kaiser, et al. Rethinking attention with performers. *International Conference on Learning Representations*, 2020. 3, 12
- [6] MMSegmentation Contributors. MMSegmentation: Openmmlab semantic segmentation toolbox and benchmark. <https://github.com/open-mmlab/mms Segmentation>, 2020. 6, 7
- [7] Ekin D Cubuk, Barret Zoph, Jonathon Shlens, and Quoc V Le. Randaugment: Practical automated data augmentation with a reduced search space. In *2020 IEEE/CVF Conference on Computer Vision and Pattern Recognition Workshops (CVPRW)*, pages 18613–18624, 2019. 5
- [8] Tri Dao and Albert Gu. Transformers are ssm: Generalized models and efficient algorithms through structured state space duality. *International Conference on Machine Learning*, 2024. 1, 2, 3, 4, 12, 14
- [9] Jia Deng, Wei Dong, Richard Socher, Li-Jia Li, Kai Li, and Li Fei-Fei. Imagenet: A large-scale hierarchical image database. In *2009 IEEE Conference on Computer Vision and Pattern Recognition*, pages 248–255. IEEE, 2009. 5
- [10] Yuchen Duan, Weiyun Wang, Zhe Chen, Xizhou Zhu, Lewei Lu, Tong Lu, Yu Qiao, Hongsheng Li, Jifeng Dai, and Wenhui Wang. Vision-rwkv: Efficient and scalable visual perception with rwkv-like architectures. In *International Conference on Learning Representations*, pages 83166–83182, 2024. 12
- [11] Qihang Fan, Huaibo Huang, and Ran He. Breaking the low-rank dilemma of linear attention. In *Computer Vision and Pattern Recognition*, pages 25271–25280, 2024. 2, 12
- [12] Yunxiang Fu, Meng Lou, and Yizhou Yu. Segman: Omni-scale context modeling with state space models and local attention for semantic segmentation. In *Computer Vision and Pattern Recognition*, pages 19077–19087, 2024. 2, 13
- [13] Riccardo Grazi, Julien N. Siems, Jorg K. H. Franke, Arber Zela, Frank Hutter, and M. Pontil. Unlocking state-tracking in linear rnns through negative eigenvalues. In *International Conference on Learning Representations*, pages 36565–36597, 2024. 2, 12
- [14] Albert Gu and Tri Dao. Mamba: Linear-time sequence modeling with selective state spaces. *arXiv.org*, 2023. Presented at International Conference on Machine Learning (ICML). 1, 2, 3, 4, 12
- [15] Albert Gu, Karan Goel, and Christopher Ré. Efficiently modeling long sequences with structured state spaces. In *International Conference on Learning Representations*, 2021. 2, 3, 12
- [16] Dongchen Han, Xuran Pan, Yizeng Han, Shiji Song, and Gao Huang. Flatten transformer: Vision transformer using focused linear attention. In *IEEE International Conference on Computer Vision*, pages 5938–5948. IEEE, 2023. 12
- [17] Dongchen Han, Ziyi Wang, Zhuofan Xia, Yizeng Han, Yifan Pu, Chunjiang Ge, Jun Song, Shiji Song, Bo Zheng, and Gao Huang. Demystify mamba in vision: A linear attention perspective. *Neural Information Processing Systems*, pages 127181–127203, 2024. 2, 12
- [18] Ali Hassani, Steven Walton, Jiachen Li, Shen Li, and Humphrey Shi. Neighborhood attention transformer. In *Computer Vision and Pattern Recognition*, 2022. 6
- [19] Ali Hatamizadeh and Jan Kautz. Mambavision: A hybrid mamba-transformer vision backbone. In *Computer Vision and Pattern Recognition*, pages 25261–25270, 2024. 2, 13
- [20] Kaiming He, Georgia Gkioxari, Piotr Dollár, and Ross B. Girshick. Mask r-cnn. In *ICCV*, 2017. 5, 6
- [21] Yi-Kuan Hsieh, Jun-Wei Hsieh, Xin Li, Ming-Ching Chang, and Yu-Chee Tseng. Partial ring scan: Revisiting scan order in vision state space models. *arXiv.org*, 2026. 2, 12
- [22] Gao Huang, Yu Sun, Zhuang Liu, Daniel Sedra, and Kilian Q Weinberger. Deep networks with stochastic depth. In *European Conference on Computer Vision*, pages 646–661. Springer International Publishing, 2016. 5
- [23] Tao Huang, Xiaohuan Pei, Shan You, Fei Wang, Chen Qian, and Chang Xu. Localmamba: Visual state space model with windowed selective scan. *ECCV Workshops*, 2024. 1, 2, 6, 7, 8, 12
- [24] Angelos Katharopoulos, Apoorv Vyas, Nikolaos Pappas, and François Fleuret. Transformers are rnns: Fast autoregressive transformers with linear attention. In *International Conference on Machine Learning*, 2020. 2, 3, 12
- [25] Aakash Lahoti, Kevin Y. Li, Berlin Chen, Caitlin Wang, Aviv Bick, J. Kolter, Tri Dao, and Albert Gu. Mamba-3: Improved sequence modeling using state space principles. In *arXiv.org*, 2026. 1, 2, 3, 12
- [26] Tanzhe Li, Caoshuo Li, Jiayi Lyu, Hongjuan Pei, Baochang Zhang, Taisong Jin, and Rongrong Ji. Damamba: Vision state space model with dynamic adaptive scan. *arXiv.org*, 38: 39777–39799, 2025. 2, 12

- [27] Tsung-Yi Lin, M. Maire, Serge J. Belongie, James Hays, P. Perona, Deva Ramanan, Piotr Dollár, and C. L. Zitnick. Microsoft coco: Common objects in context. In *European Conference on Computer Vision*, pages 740–755. Springer International Publishing, 2014. 6, 7
- [28] Tsung-Yi Lin, Piotr Dollár, Ross B. Girshick, Kaiming He, Bharath Hariharan, and Serge J. Belongie. Feature pyramid networks for object detection. In *Computer Vision and Pattern Recognition*, pages 2117–2125, 2016. 5
- [29] Weifeng Lin, Ziheng Wu, Jiayu Chen, Jun Huang, and Lianwen Jin. Scale-aware modulation meet transformer. In *IEEE International Conference on Computer Vision*, pages 5992–6003. IEEE, 2023. 6
- [30] Leiye Liu, Miao Zhang, Jihao Yin, Tingwei Liu, Wei Ji, Yongri Piao, and Huchuan Lu. Defmamba: Deformable visual state space model. In *Computer Vision and Pattern Recognition*, pages 8838–8847. IEEE, 2025. 2, 12
- [31] Yue Liu, Yunjie Tian, Yuzhong Zhao, Hongtian Yu, Lingxi Xie, Yaowei Wang, Qixiang Ye, and Yunfan Liu. Vmamba: Visual state space model. In *Neural Information Processing Systems*, pages 103031–103063. Neural Information Processing Systems Foundation, Inc. (NeurIPS), 2024. 1, 2, 6, 7, 8, 12, 13
- [32] Ze Liu, Yutong Lin, Yue Cao, Han Hu, Yixuan Wei, Zheng Zhang, Stephen Lin, and Baining Guo. Swin transformer: Hierarchical vision transformer using shifted windows. In *IEEE International Conference on Computer Vision*, pages 9992–10002. IEEE, 2021. 6, 7
- [33] Zhuang Liu, Hanzi Mao, Chao-Yuan Wu, Christoph Feichtenhofer, Trevor Darrell, and Saining Xie. A convnet for the 2020s. In *Computer Vision and Pattern Recognition*, pages 11966–11976. IEEE, 2022. 5, 6, 7
- [34] Ilya Loshchilov and Frank Hutter. Decoupled weight decay regularization. In *International Conference on Learning Representations*, 2017. 5
- [35] Meng Lou, Yunxiang Fu, and Yizhou Yu. A2mamba: Attention-augmented state space models for visual recognition. *arXiv.org*, 2025. 2, 13
- [36] Wenjie Luo, Yujia Li, Raquel Urtasun, and Richard S. Zemel. Understanding the effective receptive field in deep convolutional neural networks. In *Neural Information Processing Systems*, 2016. 7
- [37] William Merrill, Jackson Petty, and Ashish Sabharwal. The illusion of state in state-space models. *International Conference on Machine Learning*, 2024. 2, 12
- [38] Eric Nguyen, Karan Goel, Albert Gu, G. Downs, Preety Shah, Tri Dao, S. Baccus, and C. Ré. S4nd: Modeling images and videos as multidimensional signals with state spaces. *Neural Information Processing Systems*, pages 2846–2861, 2022. 12
- [39] Badri N Patro and Vijay S Agneeswaran. Hamsa: Scanning-free vision state space models via spectralpulsenet. In *arXiv.org*, pages 2408–2418, 2026. 2, 12
- [40] Xiaohuan Pei, Tao Huang, and Chang Xu. Efficientvmamba: Atrous selective scan for light weight visual mamba. *AAAI Conference on Artificial Intelligence*, 2024. 2, 7, 12
- [41] Ilija Radosavovic, Raj Prateek Kosaraju, Ross B. Girshick, Kaiming He, and Piotr Dollár. Designing network design spaces. In *Computer Vision and Pattern Recognition*, pages 10425–10433. IEEE, 2020. 6
- [42] Abdelrahman Shaker, Syed Talal Wasim, Salman Khan, Juer-gen Gall, and Fahad Shahbaz Khan. Groupmamba: Efficient group-based visual state space model. In *Computer Vision and Pattern Recognition*, pages 14912–14922, 2024. 2, 12
- [43] Yuheng Shi, Minjing Dong, Mingjia Li, and Chang Xu. Vssd: Vision mamba with non-causal state space duality. *IEEE International Conference on Computer Vision*, 2024. 1, 2, 5, 6, 7, 8, 12, 13, 14
- [44] Yuheng Shi, Minjing Dong, and Chang Xu. Multi-scale vmamba: Hierarchy in hierarchy visual state space model. *Neural Information Processing Systems*, pages 25687–25708, 2024. 2, 6, 7, 12
- [45] Jianlin Su, Yu Lu, Shengfeng Pan, Bo Wen, and Yunfeng Liu. Roformer: Enhanced transformer with rotary position embedding. *Neurocomputing*, 568:127063, 2021. 4
- [46] Christian Szegedy, Vincent Vanhoucke, Sergey Ioffe, Jon Shlens, and Zbigniew Wojna. Rethinking the inception architecture for computer vision. In *Computer Vision and Pattern Recognition*, pages 2818–2826, 2015. 5
- [47] Mingxing Tan and Quoc Le. Efficientnet: Rethinking model scaling for convolutional neural networks. In *International Conference on Machine Learning*, 2019. 6
- [48] Hugo Touvron, Matthieu Cord, Matthijs Douze, Francisco Massa, Alexandre Sablayrolles, and Herve Jegou. Training data-efficient image transformers & distillation through attention. In *International Conference on Machine Learning*, pages 10347–10357. PMLR, 2020. 5
- [49] Hugo Touvron, M. Cord, Alexandre Sablayrolles, Gabriel Synnaeve, and Hervé Jégou. Going deeper with image transformers. In *IEEE International Conference on Computer Vision*, pages 32–42. IEEE, 2021. 5
- [50] Nhat Thanh Tran, Fanghui Xue, Shuai Zhang, Jiancheng Lyu, Yunling Zheng, Yingyong Qi, and Jack Xin. Sema: a scalable and efficient mamba like attention via token localization and averaging. *arXiv.org*, 2025. 2, 12
- [51] Wenhai Wang, Enze Xie, Xiang Li, Deng-Ping Fan, Kaitao Song, Ding Liang, Tong Lu, Ping Luo, and Ling Shao. Pvt v2: Improved baselines with pyramid vision transformer. *Computational Visual Media*, 2021. 6
- [52] Chaodong Xiao, Ming-hui Li, Zhengqiang Zhang, Deyu Meng, and Lei Zhang. Spatial-mamba: Effective visual state space models via structure-aware state fusion. In *International Conference on Learning Representations*, pages 73777–73795, 2024. 2, 12
- [53] Tete Xiao, Yingcheng Liu, Bolei Zhou, Yuning Jiang, and Jian Sun. Unified perceptual parsing for scene understanding. In *European Conference on Computer Vision*, pages 432–448. Springer International Publishing, 2018. 5, 6, 7
- [54] Fei Xie, Weijia Zhang, Zhongdao Wang, and Chao Ma. Quadmamba: Learning quadtree-based selective scan for visual state space model. *Neural Information Processing Systems*, 37:117682–117707, 2024. 2, 12
- [55] Chenhongyi Yang, Zehui Chen, Miguel Espinosa, Linus Ericsson, Zhenyu Wang, Jiaming Liu, and Elliot J. Crowley. Plainmamba: Improving non-hierarchical mamba in visual

- recognition. In *British Machine Vision Conference*. BMVA, 2024. [2](#), [12](#), [13](#), [14](#)
- [56] Songlin Yang, Bailin Wang, Yikang Shen, Rameswar Panda, and Yoon Kim. Gated linear attention transformers with hardware-efficient training. *International Conference on Machine Learning*, 2023. [12](#)
- [57] Songlin Yang, Jan Kautz, and Ali Hatamizadeh. Gated delta networks: Improving mamba2 with delta rule. In *International Conference on Learning Representations*, pages 29687–29707, 2024. [12](#)
- [58] Masakazu Yoshimura, Teruaki Hayashi, Yuki Hoshino, Wei-Yao Wang, and Takeshi Ohashi. Sf-mamba: Rethinking state space model for vision. *arXiv.org*, 2026. [2](#), [12](#)
- [59] Weihao Yu and Xinchao Wang. Mambaout: Do we really need mamba for vision? *Computer Vision and Pattern Recognition*, 2024. [2](#), [6](#), [13](#)
- [60] Sangdoon Yun, Dongyoon Han, Seong Joon Oh, Sanghyuk Chun, Junsuk Choe, and Youngjoon Yoo. Cutmix: Regularization strategy to train strong classifiers with localizable features. In *IEEE International Conference on Computer Vision*, pages 6022–6031. IEEE, 2019. [5](#)
- [61] Hongyi Zhang, Moustapha Cissé, Yann Dauphin, and David Lopez-Paz. mixup: Beyond empirical risk minimization. In *International Conference on Learning Representations*, 2017.
- [62] Zhun Zhong, Liang Zheng, Guoliang Kang, Shaozi Li, and Yi Yang. Random erasing data augmentation. In *AAAI Conference on Artificial Intelligence*, pages 13001–13008, 2017. [5](#)
- [63] Bolei Zhou, Hang Zhao, Xavier Puig, Sanja Fidler, Adela Barriuso, and Antonio Torralba. Scene parsing through ade20k dataset. In *Computer Vision and Pattern Recognition*, pages 5122–5130. IEEE, 2017. [6](#), [7](#)
- [64] Lei Zhu, Xinjiang Wang, Zhanghan Ke, Wayne Zhang, and Rynson Lau. Biformer: Vision transformer with bi-level routing attention. In *Computer Vision and Pattern Recognition*, pages 10323–10333. IEEE, 2023. [6](#)
- [65] Lianghui Zhu, Biao Liao, Qian Zhang, Xiang Wang, Chunyuan Liu, and Xiaowei Zhang. Vision mamba: Efficient visual representation learning with bidirectional state space model. In *International Conference on Machine Learning*, 2024. [1](#), [2](#), [6](#), [12](#)

A. Supplementary Material

A.1. Additional Related Work

A.1.1. Vision State-Space Backbones and the Scanning Problem

State-space models (SSMs) provide a linear-complexity alternative to self-attention for long-range sequence modeling, beginning with structured SSMs such as S4 and later selective models such as Mamba and Mamba-2/SSD [8, 14, 15]. Their extension to vision has produced a rapidly growing family of visual backbones. S4ND first explored multidimensional state-space modeling for visual signals [38], while ViM, VMamba, LocalMamba, EfficientVMamba, PlainMamba, and Multi-Scale VMamba established that Mamba-style token mixers can compete with CNNs and Vision Transformers on classification and dense prediction [23, 31, 40, 44, 55, 65]. However, most of these models inherit the causal one-dimensional recurrence of sequence models: images are flattened into token sequences, processed along horizontal, vertical, local, or multi-directional scan paths, and then re-assembled into two-dimensional feature maps. These scan routes partially compensate for missing future-token context, but they also impose an artificial spatial order that is not intrinsic to images.

A second line of work improves the scan itself rather than removing it. DAMamba learns input-adaptive scan orders and regions, DefMamba introduces deformable scan paths, QuadMamba uses quadtree-based selective scanning, and GroupMamba partitions channels into grouped directional scans with post-hoc channel affinity modulation [26, 30, 42, 54]. SF-Mamba further revisits the efficiency of visual Mamba by retaining a unidirectional causal scan while routing future-to-past information through swapped auxiliary tokens and improving GPU utilization through batch folding [58]. These designs demonstrate that scan order is a central bottleneck in vision SSMs, yet they still treat visual modeling as an ordered traversal problem. In contrast, VNCT removes the traversal itself: NC-M3 aggregates over all image tokens through a scan-order-independent non-causal operator, so there is no learned, handcrafted, swapped, or deformable scan path to optimize.

A.1.2. Scan-Free and Non-Causal Vision SSMs

The closest line of work to VNCT explores whether the causal mask in visual SSMs can be removed. VSSD introduced a non-causal form of State Space Duality for vision, replacing token-wise causal hidden states with a shared global state and showing that explicit scan routes are not necessary for strong visual performance [43]. However, VSSD is built from first-order Mamba-2/SSD dynamics and uses a SISO-style state parameterization, whereas VNCT lifts Mamba-3’s second-order exponential-trapezoidal dynamics into a non-causal visual operator and further introduces low-

rank MIMO state mixing.

Several recent methods reduce or bypass scanning through other mechanisms. Spatial-Mamba keeps a single causal scan and restores two-dimensional structure through local state fusion with dilated depthwise convolutions [52]; Mamba2D derives a native two-dimensional recurrence but still evaluates it through a causal wavefront scan [2]; PRIS-Mamba averages tokens within concentric rings but retains a residual radial scan across rings [21]. Other scan-free designs move away from state-space recurrence: SEMA combines local window attention with a global arithmetic average of value tokens [50], while HAMSA replaces the SSM recurrence with FFT-domain spectral mixing [39]. DensePercept-NCSSD extends non-causal SSD ideas to dense perception tasks such as optical flow and disparity estimation [1]. These works support the broader conclusion that images need not be processed through directional recurrence, but differ in what replaces the scan. VNCT instead preserves an SSM interpretation by parameterizing global aggregation through second-order state-space coefficients.

A.1.3. SSM Operator Expressivity and Second-Order Dynamics

The connection between SSMs and attention has become increasingly explicit. Mamba-2 formulated selective SSMs through State Space Duality as structured masked matrix mixers [8], while Mamba-3 introduced exponential-trapezoidal discretization, complex-valued state updates, and a MIMO formulation [25]. VNCT adopts this second-order viewpoint but reformulates the recurrence as a non-causal aggregation operator for images.

Recent theoretical and empirical studies suggest that richer transition operators improve SSM expressivity. Merrill et al. analyze limitations of diagonal first-order SSMs, while negative-eigenvalue formulations expand state-tracking capability in linear recurrent models [13, 37]. Gated DeltaNet further enriches Mamba-style operators through delta-rule memory updates [57]. VNCT is complementary to these directions, exploring second-order trapezoidal dynamics within a scan-free non-causal visual formulation.

A.1.4. Efficient Global Mixing, Linear Attention, and Hybrid Designs

Because VNCT factorizes global source statistics followed by per-token readout, it is algebraically related to linear attention [5, 24], consistent with recent analyses relating Mamba-style models to kernelized attention [17]. Unlike conventional linear attention, however, VNCT parameterizes its kernel using data-dependent SSM discretization coefficients, including the trapezoidal α, β, γ parameters.

Efficient global mixers such as FLatten, Gated Linear Attention, Vision-RWKV, and RALA improve linear token mixing through focused kernels, gating, recurrent mixing, or rank augmentation [10, 11, 16, 56]. VNCT instead intro-

duces cross-channel interaction through a low-rank MIMO state-space formulation. Hybrid architectures including MambaVision, SegMAN, and A2Mamba combine SSMS with attention modules [12, 19, 35], whereas MambaOut questions whether SSM recurrence itself is necessary for visual recognition [59]. VNCT takes a different perspective: the limitation lies in directional scanning rather than state-space modeling, motivating a second-order non-causal formulation with attention restricted to the final low-resolution stage.

A.2. Notation

Let $\mathbf{X} = [\mathbf{x}_1, \dots, \mathbf{x}_L]^\top \in \mathbb{R}^{L \times C}$ denote a sequence of L image tokens with channel dimension C , obtained by flattening a spatial feature map of resolution $H \times W$, so that $L = HW$. We index tokens with i (target) and j (source), and channels with c . Vectors are bold lowercase; matrices and tensors are bold uppercase. Throughout, we treat each channel independently when deriving scalar-valued aggregation expressions, then lift to the full channel dimension by broadcasting.

The following additional symbols are used consistently: N denotes the SSM state dimension, H the number of SSM heads, R the MIMO rank, $d_{\text{head}} = d_{\text{inner}}/H$ the per-head feature dimension with $d_{\text{inner}} = 2C$ by default, and S the number of RoPE angle dimensions.

A.3. Causal Bias Analysis: Why Lower-Triangular Structure Is Problematic for Vision

To understand the motivation concretely, consider unrolling Eq. (3) over L steps. For a single channel c , defining $\tilde{x}_{j,c} = b_{j,c} x_{j,c}$, the causal state sequence is described by a lower-triangular linear map

$$\mathbf{h}_c = \mathbf{M}_c \tilde{\mathbf{x}}_c, \quad (26)$$

where $\mathbf{h}_c, \tilde{\mathbf{x}}_c \in \mathbb{R}^L$ collect per-position states and weighted observations, and $\mathbf{M}_c \in \mathbb{R}^{L \times L}$ is the transition matrix with $M_{ij,c} = 0$ whenever $j > i$. For a two-dimensional image flattened into a one-dimensional sequence, this triangular structure has no relationship to spatial proximity: two adjacent pixels separated by the scan fold contribute asymmetrically to each other’s state, while two distant tokens on the same scan-row interact more strongly than geometrically closer tokens on different rows. Multi-directional approaches [31] mitigate this by averaging over multiple lower-triangular maps, but each individual map remains lower-triangular and their average does not achieve permutation invariance. The non-causal lift replaces \mathbf{M}_c with a dense, symmetric interaction matrix derived from the same parameters α, β, γ .

A.4. 2D RoPE: Full Derivation and Implementation

For a token at grid position (r_i, c_i) , the phase vector is

$$\varphi_i = \begin{bmatrix} r_i f_{h,1}, \dots, r_i f_{h,S/2}, \\ c_i f_{w,1}, \dots, c_i f_{w,S/2} \end{bmatrix} \in \mathbb{R}^S, \quad (27)$$

where $f_{h,k} = f_{w,k} = 10000^{-2(k-1)/S}$ are the standard sinusoidal frequency terms. The rotation is applied to adjacent pairs in the last dimension:

$$\tilde{B}_{i,r,s} = B_{i,r,s} \cos \varphi_{i,s} - B_{i,r,s+S/2} \sin \varphi_{i,s}, \quad (28)$$

and symmetrically for \mathbf{C} , where r indexes MIMO rank and s indexes the phase dimension. The inner product $\tilde{\mathbf{B}}_{j,r}^\top \tilde{\mathbf{C}}_{i,r}$ that appears implicitly in the aggregation einsum becomes

$$\tilde{\mathbf{B}}_{j,r}^\top \tilde{\mathbf{C}}_{i,r} = \sum_{s=1}^{S/2} \begin{bmatrix} B_{j,r,s} C_{i,r,s} \cos(\varphi_{j,s} - \varphi_{i,s}) \\ + B_{j,r,s} C_{i,r,s+S/2} \sin(\varphi_{j,s} - \varphi_{i,s}) \\ + \dots \end{bmatrix}, \quad (29)$$

which depends on phase differences $\varphi_{j,s} - \varphi_{i,s}$, encoding relative spatial displacement. Crucially, after rotation $\tilde{\mathbf{B}}$ depends only on source index j and $\tilde{\mathbf{C}}$ only on target index i , so the global statistics \mathbf{S}_c and \mathbf{Z}_c can still be accumulated in a single pass. In implementation, phases are computed from the actual (H, W) grid dimensions at each stage. The remaining dimensions of \mathbf{B} and \mathbf{C} beyond S phase pairs are left unrotated.

A.5. Scan Invariance vs. Direction Invariance

Two related but distinct properties appear in the scan-free vision SSM literature. *Direction invariance* means the output representation is insensitive to the orientation of a scan: rotating or reflecting the scan pattern leaves the representation unchanged. This is approximately achieved by averaging over multiple fixed scan directions, as in VMamba [31] (four directions) or PlainMamba [55] (continuous 2D scanning). Direction invariance does not imply invariance to arbitrary token permutations. *Scan invariance* is the strictly stronger property that the output is invariant to any permutation of the input token sequence. NC-M3 achieves scan invariance by construction: the accumulation in Eqs. (17)–(18) is a commutative sum and the readout draws from the same global \mathbf{G} for every target token. Direction-invariant methods may exhibit residual anisotropy in effective receptive field (ERF) patterns [43], whereas scan-invariant methods have isotropic ERFs by construction, which is advantageous for boundary detection and small-object segmentation. Spatial structure is re-introduced into NC-M3 through 2D RoPE (relative position) and Pos2D (absolute position), consistent

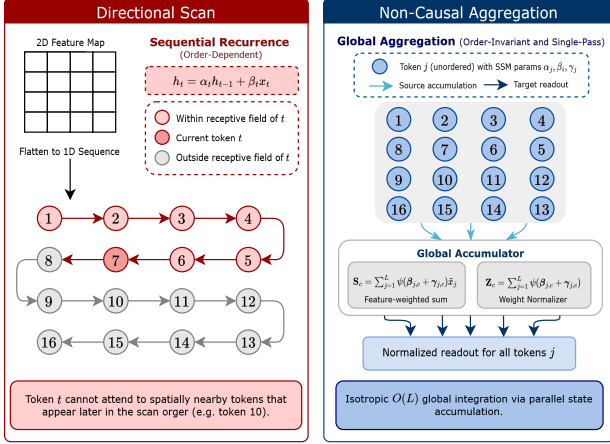


Figure 5. **Directional scanning versus non-causal aggregation.** Existing vision SSMs impose one or more fixed scan orders over the token grid (e.g. horizontal, vertical, or multi-directional), introducing an artificial sequential ordering that is not intrinsic to images. NC-M3 instead aggregates all tokens into a single shared global state that every token reads back, eliminating scan order entirely while preserving linear-time complexity.

with VSSD [43] and PlainMamba [55]. Figure 5 contrasts the two regimes: directional vision SSMs traverse the token grid along one or more fixed scan orders, whereas NC-M3 replaces every such traversal with a single permutation-invariant aggregation into a shared global state that all tokens read back.

A.6. MIMO: Extended Analysis

The parameter and computational cost of MIMO is $\mathcal{O}(HRd_{\text{head}}) = \mathcal{O}(CR)$ for the mixing tensor \mathbf{U} , compared to $\mathcal{O}(C^2)$ for a full cross-channel linear map. For typical values ($R = 4$, $C = 96\text{--}768$), this represents a parameter reduction of $24\times$ to $192\times$ relative to a full mixing layer. Without MIMO ($R = 1$), the aggregation reduces to the standard SISO form and \mathbf{U} degenerates to a per-head identity.

A.7. Memory-Efficient Implementation

To avoid materializing the full $(B, L, H, d_{\text{head}}, R, N)$ intermediate tensor, both Eqs. (17) and (18) are evaluated in chunks of K tokens along the spatial dimension, requiring $\mathcal{O}(K \cdot H \cdot d_{\text{head}} \cdot R \cdot N)$ peak memory per chunk. The chunk size K is set adaptively based on model width: $K = 256$ for micro and tiny variants, $K = 128$ for small, and $K = 32$ for base, calibrated to keep peak per-chunk memory below 150 MB on A100-40 GB at the respective batch sizes.

The step-size bias $b_{\Delta, h}$ in Eq. (11) is initialized following the Mamba-2 strategy [8] to encourage moderate initial step sizes.

A.8. Hierarchical Design Rationale

The motivation for hierarchical processing is twofold. First, dense prediction tasks require features at multiple scales: fine-grained spatial detail at high resolution for precise boundary localization and abstract semantic content at low resolution for region classification. Second, hierarchical processing enables NC-M3 to work at progressively smaller sequence lengths in deeper stages; at lower resolutions, each token represents a larger spatial region and aggregation across all tokens captures broader context with higher signal-to-noise ratio.

The LPU serves a secondary purpose beyond injecting local inductive bias: by providing each token with awareness of its immediate neighborhood prior to RoPE-based global aggregation, it reduces the burden on the positional encoding to capture short-range dependencies.

A.9. VNCT Backbone Configurations

Table 9 summarizes the backbone configurations of all VNCT variants. All models share the same architecture shown in Fig. 2: Stages 1–3 employ VNCT (NC-M3) blocks, while Stage 4 uses Hybrid-Attention. The variants differ only in channel dimensions, stage depths, and stochastic depth rate. Unless otherwise specified, all NC-M3 layers use a state dimension of $d_{\text{state}} = 64$.

A.10. Training Details

Unless otherwise specified, ImageNet-1K models are trained for 300 epochs using AdamW with an initial learning rate of 1×10^{-3} , weight decay of 0.05, a cosine learning-rate schedule, and a 20-epoch linear warm-up. Models are trained at 224×224 resolution with a per-GPU batch size of 128 (64 for VNCT-Base using gradient accumulation). We employ RandAugment, Mixup, CutMix, Random Erasing, and label smoothing. Exponential Moving Average (EMA) weights with a decay factor of 0.9999 are maintained throughout training, and the checkpoint with the highest validation Top-1 accuracy is used for evaluation.

For downstream object detection and instance segmentation, we adopt the official VSSD configuration using Mask R-CNN in MMDetection under the standard $1\times$ and $3\times$ schedules. Semantic segmentation follows the official UPerNet configuration in MMSegmentation. All downstream experiments initialize the backbone from the corresponding ImageNet-1K pretrained checkpoint while keeping all optimization settings identical to the VSSD baseline.

A.11. Extended Ablation Studies

Unless otherwise specified, all ablation studies are conducted using the VNCT-T backbone. This appendix provides detailed analyses of the architectural choices summarized in the main paper, including non-causal aggregation, second-order

Table 9. **VNCT backbone configurations.** Stage resolutions are fixed at $\{H/4, H/8, H/16, H/32\}$ for all variants.

Variant	Stage Channels	Stage Depths	Drop Path
VNCT-Micro	{64, 128, 256, 512}	{2, 2, 6, 2}	0.1
VNCT-Tiny	{96, 192, 384, 768}	{2, 2, 9, 2}	0.2
VNCT-Small	{96, 192, 384, 768}	{3, 3, 18, 3}	0.3
VNCT-Base	{128, 256, 512, 1024}	{3, 3, 27, 3}	0.5

Table 10. **Effect of non-causal aggregation.**

Metric	Scan-based	Non-causal
Top-1 (%)	83.5	84.2
COCO AP	46.4	47.8
ADE mIoU	47.6	48.8
Boundary IoU	48.9	50.8

Table 11. **Effect of second-order dynamics.**

Metric	First-order	Second-order
Top-1 (%)	83.6	84.2
ADE mIoU	47.7	48.8
Boundary IoU	49.2	50.8

dynamics, the proposed low-rank MIMO formulation, positional encoding, and comparisons with first-order non-causal state-space models.

A.12. Effect of Non-Causal Aggregation

To evaluate the role of global non-causal aggregation, we compare VNCT against a causal counterpart in which non-causal aggregation is replaced with directional scan-based recurrence while keeping all other components unchanged. As shown in Table 10, replacing directional recurrence with non-causal aggregation consistently improves performance across all evaluated tasks. The largest gains are observed on dense prediction benchmarks, particularly Boundary IoU, demonstrating that isotropic global interactions provide richer spatial context than directional scan paths.

A.13. Effect of Second-Order Dynamics

To isolate the contribution of the proposed exponential-trapezoidal formulation, we replace the second-order update with a first-order Euler approximation while keeping the remaining architecture unchanged. Results in Table 11 show consistent improvements across both classification and dense prediction tasks. In particular, the larger gain in Boundary IoU suggests that second-order dynamics better preserve fine spatial structures and object boundaries by capturing richer state evolution.

Table 12. **Effect of the low-rank MIMO formulation.**

Metric	SISO	MIMO
Top-1 (%)	83.8	84.2
COCO AP	47.0	47.8
ADE mIoU	48.0	48.8
Boundary IoU	49.5	50.8

A.14. Effect of the Low-Rank MIMO Formulation

To assess the effectiveness of the proposed low-rank MIMO parameterization, we replace it with a single-input single-output (SISO) formulation while preserving the same model capacity wherever possible. As reported in Table 12, jointly modeling spatial and channel-wise interactions consistently improves performance across all benchmarks.

A.15. Effect of Positional Encoding

Since non-causal aggregation does not impose an inherent ordering over tokens, positional information plays an important role in modeling spatial relationships. We compare several positional encoding strategies, including no positional encoding, 2D sinusoidal encoding, RoPE, and their combination. As shown in Table 13, combining 2D sinusoidal encoding with RoPE yields the strongest results, suggesting that the two encoding schemes provide complementary spatial cues.

Table 13. **Effect of positional encoding.**

Variant	Top-1	ADE mIoU
None	82.9	46.8
2D Sinusoidal	83.7	48.0
RoPE	83.8	48.1
2D Sinusoidal + RoPE	84.2	48.8

A.16. Comparison with First-Order Non-Causal State-Space Models

We directly compare VNCT-T with the first-order non-causal VSSD-T baseline under identical training and evaluation settings. As summarized in Table 14, the proposed second-order formulation consistently outperforms its first-order counterpart across all benchmarks. The largest improvements are observed on dense prediction tasks, with gains of +0.9 AP, +0.9 mIoU, and +3.7 Boundary IoU, indicating

Table 14. **First-order versus second-order non-causal state-space models.**

Metric	VSSD-T	VNCT-T
Top-1 (%)	83.7	84.2
COCO AP	46.9	47.8
ADE mIoU	47.9	48.8
Boundary IoU	49.1	50.8

that second-order state dynamics provide a more expressive representation for capturing complex spatial dependencies.